A Stochastically Homogenized Peridynamic Model for Intraply Fracture in Fiber-Reinforced Composites

Javad Mehrmashhadi [a], Ziguang Chen [b, *], Jiangming Zhao [a], Florin Bobaru [a, *]

[a] University of Nebraska-Lincoln, Lincoln, NE 68588, United States

[b] Huazhong University of Science and Technology, Wuhan 430074, China

* Email of Corresponding Authors: fbobaru2@unl.edu, zchen@hust.edu.cn

Abstract

The quasi-static transverse fracture behavior in unidirectional fiber-reinforced composites (FRCs) is investigated using a new intermediately-homogenized peridynamic (IH-PD) model and a fully homogenized peridynamic (FH-PD) model. The novelty in the IH-PD model here is accounting for the topology of the fiber-phase in the transverse sample loading via a calibration to the Halpin-Tsai model. Both models can capture well the measured load-displacement behavior observed experimentally for intraply fracture, without the need for an explicit representation of microstructure geometry of the FRC. The IH-PD model, however, is more accurate and produces crack path tortuosity as well as a non-monotonic load-crack-opening softening curve, similar to what is observed experimentally. These benefits come from the preservation of some micro-scale heterogeneity, stochastically generated in the IH-PD model to match the composite's fiber volume fraction, while its computational cost is equivalent to that of an FH-PD model. We also present a three-point bending transverse loading case in which the two models lead to dramatically different failure modes: the FH-PD model shows that failure always starts from the off-center pre-notch, while the IH-PD model, when the pre-notch is sufficiently off-center, finds that the composite fails from the center of the sample, not from the pre-notch. Experiments that can confirm these findings are sought.

Keywords: Fiber-reinforced composites, Homogenization, Peridynamics, Transverse fracture, Crack path

1. Introduction

Understanding fracture and failure in fiber-reinforced composites (FRCs) are essential for the design of composite parts with increased fracture toughness. A major precursor to catastrophic failure of FRCs, usually induced by intralaminar fracture, is the fracture that occurs transverse to the lamina plane, via matrix cracking and fiber-matrix debonding [1]. These types of cracks that propagate under transverse loading conditions of a ply are called transverse intralaminar (or intraply) cracks. Given the size of the reinforcing fibers relative to the size of a composite structure, performing fracture simulations with the explicit microstructure geometry is not feasible. Because of this, intraply fracture has been mostly studied using homogenization techniques or the Representative Volume Element (RVE) method, which avoid using the detailed FRC microstructure geometry [2], but the results are far from satisfactory. Attempts to model transverse fracture using the FRC microstructure produce realisitc results but work only for samples

of reduced size [3]. Here we present a model that does not require the detailed microstructure of the composite yet it leads to fracture results similar to those that do.

The homogenization theory for composites is a well-established, efficient and accurate methodology to compute the elastic behavior for composites from the properties and spatial distribution of the different constituent phases [4, 5]. Homogenization incorporates experimental or analytical methods to determine the model parameters, which include the effect of fibers [3, 6-8]. Nevertheless, the extension to the non-linear regime, and particularly to situations involving strain localization and fracture, is more complex and the results' correctness is not always guaranteed [9].

Models using the explicit FRC microstructure to study fracture behavior of different types of fiber-reinforced materials have appeared in, for example, [10-16]. Simulating the detailed microstructure at the structural scale is not computationally feasible [17]. Approaches using RVEs with Cohesive Zone Model (CZM) to simulate fracture behavior ([15-20]) may not always be applicable to cases with arbitrary loading conditions because the validity of an RVE for fracture problems is questionable. To allow modeling of larger samples while making use of the explicit microstructure to capture the fracture behavior, attempts have been made to combine a homogenized model with a small area of explicit microstructure geometry representation near the location where cracks initiate and grows through [21]. Using such an approach, one can simulate intraply fracture growing from a pre-notch in a transversely loaded FRC under three-point bend test [21]. This combination between homogenization and explicit microstructure modeling is possible only when the damage region is known in advance and is efficient only if damage is limited to a small area of the entire sample.

Recent studies of deformation and damage under *transverse loading* in FRC structures used the Finite Element Method (FEM) [6, 21, 22], phase-field approaches [23] and peridynamics [24]. To be able to predict crack growth in transversely loaded FRCs, models based on FEM apparently require the explicit representation of the microstructure [21]. Furthermore, crack initiation and propagation are bounded to evolve within the constraints of cohesive-zone models (along the element faces). Nonlocal models discretized with meshfree methods have been successful in predicting the observed behavior in complicated fracture and corrosion damage problems [25-29], for example. The peridynamic (PD) theory was recently used to study tensile fracture in RVEs where the explicit microstructure was modeled [30, 31]. Regular homogenization techniques, when used for fracture problems in which the microstructure plays a critical role, has been shown to fail to reproduce the experimentally observed behavior in certain cases [32]. The goal of the present contribution is to show that a special type of "homogenization" allows us to predict fracture in materials with microstructure (transversely loaded FRCs) without the detailed representation of the microstructure and at a computational cost equivalent to that of corresponding fully homogenized models.

The paper is organized as follows: in Section 2 we give a brief review of peridynamics; in Section 3 we describe the fully homogenized peridynamic (FH-PD) model and the intermediately (or partially)

homogenized peridynamic (IH-PD) model that takes into account the fiber-volume fraction; in Section 4 we study the elasticity under transverse loading with the two models and show some limitation of the IH-PD model that leads us to introduce an improved version that accounts for discontinuity of the fiber-phase in the transverse cross-section of a unidirectional FRC; the problem setting for a three-point bending test on a transversely loaded pre-notched FRC is described in section 5, while in Section 6 we compare the results from the FH-PD and IH-PD models in terms of crack path and load versus displacement curve for the three-point bending test with those from experiments; in Section 7 we show an interesting fracture case in three-point bending specimens with an asymmetric notch for which the two models show starkly different responses; conclusions and future work are given in Section 8.

2. A brief review of peridynamics

Peridynamics was introduced as a nonlocal form of continuum mechanics by Silling in 2000 [33] for modeling damage and fracture. Since then, it has been extended to a variety of other problems in which domain changes/discontinuities are part of the problem [28, 34]. In this theory, each material point is connected through peridynamic bonds to other points within a certain neighborhood region called "the horizon". The peridynamic bonds transfer forces between points (or mass or heat, as in [26, 35]) and their failure defines damage at each point. In peridynamics, one replaces the equation of motion by an integro-differential equation in which spatial derivatives are eliminated. This allows peridynamics to avoid the mathematical difficulties and inconsistencies present in the classical theory when cracks, for example, develop in the domain. The PD equations for quasi-static problems are:

$$\int_H \boldsymbol{f}(\boldsymbol{u}\,(\hat{\boldsymbol{x}},t)-\boldsymbol{u}\,(\boldsymbol{x},t),\hat{\boldsymbol{x}}-\boldsymbol{x})\,dA_{\hat{\boldsymbol{x}}}=0 \tag{1}$$

where $\boldsymbol{u}$ is the displacement vector field, and ρ is the mass density, $\boldsymbol{f}$ is the peridynamic pairwise force function that describes the interaction between material points. The horizon region is the internal sub-region H (see Fig. 1), defined as:

$$H=\left\{\hat{\boldsymbol{x}}\epsilon\Re\colon\left||\hat{\boldsymbol{x}}-\boldsymbol{x}|\right|<\delta\right\} \tag{2}$$

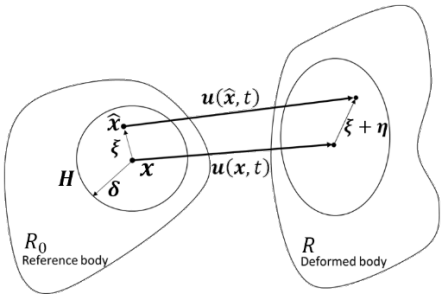

Fig. 1. The deformation of a peridynamic bond

Let $\boldsymbol{\eta}=\boldsymbol{u}\,(\hat{\boldsymbol{x}},t)-\boldsymbol{u}\,(\boldsymbol{x},t)$ be the relative displacement and $\boldsymbol{\xi}=\hat{\boldsymbol{x}}-\boldsymbol{x}$ be the relative position in the reference configuration between two material points of $\hat{\boldsymbol{x}}$ and $\boldsymbol{x}$. From Equation 2 we have $||\boldsymbol{\xi}||>\delta\Rightarrow$

$\boldsymbol{f}(\boldsymbol{\eta},\boldsymbol{\zeta}) = \mathbf{0}$. When the pairwise force derives from a micro-elastic potential w, a micro-elastic material is defined by the following interaction force:

$$\boldsymbol{f}(\boldsymbol{\eta},\boldsymbol{\xi}) = \frac{\partial w(\boldsymbol{\eta},\boldsymbol{\xi})}{\partial \boldsymbol{\eta}} \tag{3}$$

A linear micro-elastic material is obtained if we consider:

$$w(\boldsymbol{\eta},\boldsymbol{\xi}) = \frac{c(\boldsymbol{\xi})s^2||\boldsymbol{\xi}||}{2} \tag{4}$$

where $c(\boldsymbol{\xi})$ is called the bond micromodulus function and s is the relative elongation of the bond, or the bond strain:

$$s = \frac{\|\boldsymbol{\eta}+\boldsymbol{\xi}\| - \|\boldsymbol{\xi}\|}{\|\boldsymbol{\xi}\|} \tag{5}$$

The pairwise force derived from Equations 3 and 4 is:

$$\boldsymbol{f}(\boldsymbol{\eta},\boldsymbol{\xi}) = \begin{cases} \dfrac{\boldsymbol{\eta}+\boldsymbol{\xi}}{\|\boldsymbol{\eta}+\boldsymbol{\xi}\|} c(\boldsymbol{\xi})s, & |\boldsymbol{\xi}| \le \delta \\ 0, & |\boldsymbol{\xi}| > \delta \end{cases} \tag{6}$$

In this study we use plane stress conditions and the conical micromodulus (see [36]):

$$c(\boldsymbol{\xi}) = \frac{24E}{\pi\delta^3(1-\nu)}\left(1 - \frac{||\boldsymbol{\xi}||}{\delta}\right) \tag{7}$$

where *E* is the elastic Young's modulus, and ν is the Poisson ratio (fixed to 1/3 in2D plane stress with the bond-based version of PD).

In peridynamics, damage is modeled using the critical bond strain concept, allowing a bond to break and no longer sustain a force [33, 37] once its strain goes beyond a critical value. In this study, once a peridynamic bond breaks, it remains broken [26, 28]. The critical bond strain parameter is obtained from the measured fracture energy, G_0 [37]. In 2D plane stress, the connection between s_0 and G_0 is [38]:

$$G_0 = 2\int_0^{\delta}\int_z^{\delta}\int_0^{cos^{-1}(z/\xi)} [c(\boldsymbol{\xi}){s_0}^2(\boldsymbol{\xi})/2]\boldsymbol{\xi}\, d\theta\, d\boldsymbol{\xi}\, dz \tag{8}$$

For the conical micromodulus given in Equation 7, one obtains the critical strain as (see [39]):

$$s_0 = \sqrt{\frac{5\pi G_0}{9E\delta}} \tag{9}$$

Using a one-point Gaussian integration, the discrete version of Equation 1 at a node $\boldsymbol{x_i}$ is (see [40] and below):

$$\sum_{j\in H_i} \boldsymbol{f}(\boldsymbol{x}_j - \boldsymbol{x}_i, \boldsymbol{u}_j - \boldsymbol{u}_i)\Delta A_i = \mathbf{0} \tag{10}$$

where $\boldsymbol{x_j}$ are nodes inside the horizon region of $\boldsymbol{x_i}$, and ΔA_i is the nodal area (volume in 3D) of node $\boldsymbol{x_i}$. The nonlinear conjugate gradient (NCG) method is used to solve the nonlinear (in displacements) system in Equation 10. This is similar to the algorithm used in [41] and [39], except that here we use the stopping criterion presented in [42] with a more efficient hybrid conjugate gradient (CG) algorithm introduced in [43] to find β. The complete discussion of the CG method is available in [42] and is briefly shown in Appendix A.

To create the discretization grids, several options are available. Non-uniform grids (in which node density does not vary significantly over the domain so that the quadrature error is minimized) are better in modeling rounded shapes than uniform grids, and they can be easily created from finite element meshes [44]. In this work, PD nodes in the uniform and non-uniform grids are selected so that they are always located at the centroid of their nodal areas (see [45] for a discussion on other options). We use ANSYS to create non-uniform meshes: the element centroid is the PD node, and the element area is the PD nodal area. An ANSYS APDL code was created to find element centroids and element areas (see Appendix B). Schematic pictures of element centroid for uniform and non-uniform mesh are shown in Fig. 2.

Fig. 2. Element centroids for (a) a uniform part of the mesh and (b) a non-uniform part of the mesh are chosen as PD nodes. The element area is used as the PD nodal area.

3. Homogenized peridynamic models for the transverse elastic behavior of fiber-reinforced composites

We consider a unidirectional FRC loaded transversely. In this section, we briefly discuss two types of homogenization of peridynamic models for transversely loaded FRCs: the fully homogenized (FH-PD) model and intermediately homogenized (IH-PD) model. These models have been previously evaluated for wave propagation and dynamic and quasi-static fracture in functionally graded and porous materials [32].

3.1. The fully homogenized peridynamic model

Several homogenization methods have been introduced for fiber-reinforced composites to predict the elastic and fracture behavior of FRCs using peridynamics. For instance, in [46], a homogenized PD model was introduced for a unidirectional composite lamina where the composite elastic constants were formulated by matching the PD strain with the classical strain energy along certain directions. Since in the present study we focus on transversely isotropic composites (the cross-section of unidirectional FRCs), we

define a fully homogenized peridynamic (FH-PD) material model as a micro elastic material whose elastic properties are computed to match those of an equivalent homogenized classical model. Because no experimental values are available for the composites discussed in Section 4 and beyond, in this study we use the Halpin-Tsai relationships to estimate the transverse Young's modulus. Halpin-Tsai relationships have been widely used because of their accuracy in predicting the transverse and shear moduli in FRCs [17, 46-48].

Thus, the transverse Young's modulus we will match with our FH-PD model is:

$$E_{Tsai} = [1 + \xi\eta f]/[1 - \eta f]\, E_m \tag{11}$$

where,

- E_m and E_f are matrix and fiber Young's modulus, respectively.
- f is the fiber volume fraction
- $\eta = \left[E_f/E_m - 1\right]/\left[E_f/E_m + \xi\right]$
- ξ is a parameter that accounts for the packing and fiber geometry ($\xi = 2$ for fibers with square or round cross-section)

3.2. The intermediately-homogenized peridynamic model

With peridynamics, there are three types of bonds for a two-phase material model. For the transverse section of a fiber-reinforced composite, we can define [25]: fiber-fiber (F-F) PD bonds (with their micromodulus computed from the Young's modulus E_f of the fiber material, see Eq. 7), matrix-matrix (M-M) bonds (with micromodulus computed based on Young's modulus E_m of matrix material), and interface bonds, with a micromodulus set to match a Young's modulus E_{int}. For determining the mechanical properties of the interface bond, several methods of averaging like harmonic averaging, arithmetic averaging, and area-weighted averaging have been used in previous PD models [25, 32, 35]. Here, we consider the harmonic averaging method as follows:

$$E_{int}^{-1} = \frac{1}{2}(E_m^{-1} + E_f^{-1}) \tag{12}$$

In this study, we introduce an intermediately homogenized peridynamic (IH-PD) model for transversely loaded FRCs, calibrated to match the volume fractions of the phases, and using a stochastic procedure to define the mechanical properties of the PD bonds. The model does not require the FRC microstructure geometry, it only needs the volume fraction information, and is homogeneous at scales larger than the horizon size (if the material modeled is homogeneous at the larger scale). The stochastic properties of the model make it non-homogeneous at the horizon size scale, with bond properties distributed randomly to match the given volume fractions of the phases. This is the reason for naming it an "intermediately-homogenized" PD model. The IH-PD model is simpler compared with classical approaches for modeling random heterogeneity in composites [5].

We assume that the unidirectional FRC's transverse cross-section is homogeneous at the large scale, and that the volume fraction of fibers is f. In a peridynamic model discretized with the meshfree discretization (see section 4 and [33]) each PD node is associated with a certain area/volume. Assuming that the microstructural geometrical features (in our case the diameter of the fibers) are small compared with the nodal area/volume (or the horizon size, which is usually taken as 4-6 times the discretization size in applications [49, 50]), the following arguments can be made to generate a macro-scale homogenized model via a stochastic procedure. Referring to Fig. 3, the coordinates of nodes $\boldsymbol{x}$ and $\hat{\boldsymbol{x}}$ may fall over fiber or matrix material. Depending on the fiber volume fraction (f) at the nodal area of $\boldsymbol{x}$ (or $\hat{\boldsymbol{x}}$, which are the same because we assumed a macro-scale homogenous composite), the following probabilities are defined: the material point at $\boldsymbol{x}$ has the chance f, to cover fiber material and $(1-f)$ to cover matrix material. Similarly, for the material point at $\hat{\boldsymbol{x}}$. Based on these probabilities, we find the probabilities for the properties of the $\boldsymbol{x}-\hat{\boldsymbol{x}}$ bond as follows (see Fig. 3): probability f^2 to be a fiber-fiber (F-F) bond, the chance $(1-f)^2$ to be a matrix-matrix (M-M) bond, and the chance $1-f^2-(1-f)^2$ to be a fiber-matrix (F-M) or interface bond. Heterogeneity is thus maintained at the small-scale (horizon-size scale) by having stochastically-generated mechanical bonds with different material properties. The detailed algorithm showing how an IH-PD model is instantiated, as a pre-processing step, is:

I. For each node $\boldsymbol{x}$
II. For each node $\hat{\boldsymbol{x}}$ in the family of $\boldsymbol{x}$, generate a random number r in $[0,1]$ from a uniform distribution.
III. Assign properties for the bond $\boldsymbol{x}-\hat{\boldsymbol{x}}$ (as well as $\hat{\boldsymbol{x}}-\boldsymbol{x}$) as follows:
    a. If $r < f^2$, then assign the bond as F–F bond
    b. If $f^2 < r < (1-f)^2 + f^2$, then assign the bond as M-M bond
    c. Else, assign the bond as an interface bond

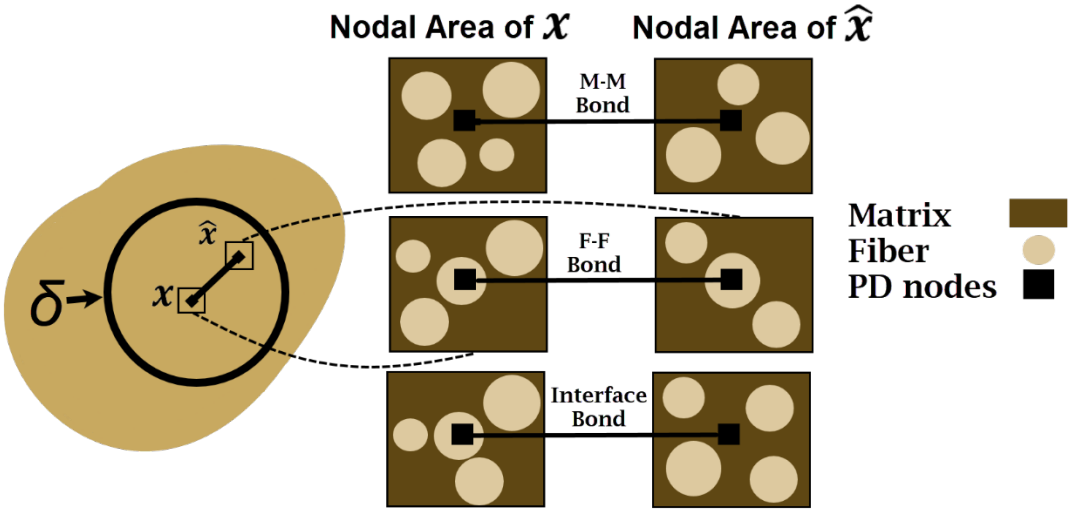

Fig. 3. The three possibilities for a bond $\boldsymbol{x}-\hat{\boldsymbol{x}}$ in the composite to be assigned its mechanical property depends on the volume fraction of the phases.

As an example of generating bond properties with the stochastic model above, in Fig. 4 we show the particular bonds computed by the algorithm for a certain node in an FRC with the fiber fraction 54%. For this fiber volume fraction, on average, at a certain node, 29.2%, 21.2%, and 49.6% of its bonds will be assigned to be F-F, M-M, and F-M bonds, respectively.

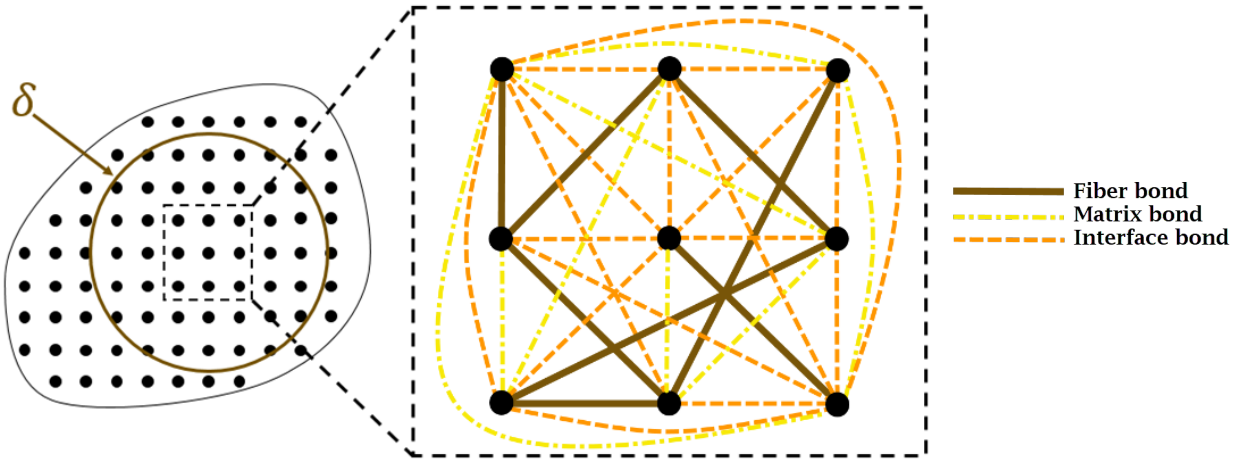

Fig. 4. An example of a possible distribution of bond assignments in the IH-PD model (only bonds between the nodes shown are drawn).

Note that the randomness generated by the IH-PD model does not consider the discontinuity between fibers. It creates a network of interpenetrating bonds with different properties. Material systems with such an interpenetrating microarchitecture exist, but the transverse cross-section of a unidirectional FRC is not one of them. The question then becomes: how important is the particular phase distribution, and in particular the connectivity of the phases, in describing the elastic and brittle fracture behavior in transversely loaded FRCs? We address this question in the next sections.

4. The composite elastic response for the IH-PD model and the Halpin-Tsai calibrated model

We first test the IH-PD model for the elastic behavior of the transverse FRC under a simple tension test. We then compare the IH-PD model elastic results in three-point bending with experiments on transverse loading for two types of FRCs: composite I (unidirectional $[0]_{14}$E-glass/MTM57 composites with fiber volume fraction of 54% [21]), and composite II (Ti-6Al-4V reinforced by SiC sigma 1140+ fibers with fiber volume fraction of 35% [51]). The material properties for these two composite systems are listed in Table I. The reasons to select these two particular systems to test the elastic behavior of the IH-PD model are their different fiber volume fractions and contrast between their fiber and matrix Young's moduli (the ratio is about 22 to 1 for composite I, and 3 to 1 for composite II).

Table I Material properties of composites I [21, 52] and II [51]. Interface Young's moduli are obtained from Equation 12.

	Composite I			Composite II
	E (GPa)	ν	Fracture Energy, G_0 (Jm^{-2})	E (GPa)
Fiber	74.0	0.2	400.0±50 (Parallel to Fibers)	330.0
Matrix	3.35	0.35	100.0	110.0
Interface	6.3	--	150.0	165.0

4.1. Verification for a simple tension test

We verify the IH-PD model against a classical homogenized model (the transverse Young's modulus from Equation 11) via a simple tension test. We first consider composite II (see Table I for material property). Here we choose a cross-section of dimensions 100×40 mm^2 with the tensile loading of 1.0 MPa on both the left and the right edge of the sample (see Fig. 5). For the classical solution, we use E_{Tsai}=164GPa, computed from Equation 11, with the fiber volume fraction of 35% and the material parameters from Table I. In the PD model, we apply equivalent loading conditions as body forces over three layers of nodes. Applying the imposed boundary conditions at one layer of nodes leads to a more pronounced peridynamic surface effect (see [45]). One way to completely remove the peridynamic surface effect, for simple geometries and loading conditions, is the fictitious node method described in [25, 45]. However, the fictitious node method for the three-point bending (and fracture) test (see section 4.2) is more complicated (and it cannot eliminate the peridynamic surface effect) and it is not used in the present work. The horizon size in the PD solutions is 2.0 mm with m-factor of 4. The relative difference in the horizontal component of displacement between the PD solution and the exact classical solution is near zero over most of the sample (see Fig. 5.a). Notice that near the middle of the sample, where the exact classical model horizontal displacements are zero, the relative difference computation is affected by the cancellation numerical error. This is the reason for the apparent higher values for the relative difference in that region. Please observe that the IH-PD model, even when solved over a uniform grid, has some small "perturbations" in the displacement contours (observable here as through the relative difference), due to the randomness of the bond "microstructure". Possible effects on the solution of IH-PD models are discussed in the following section.

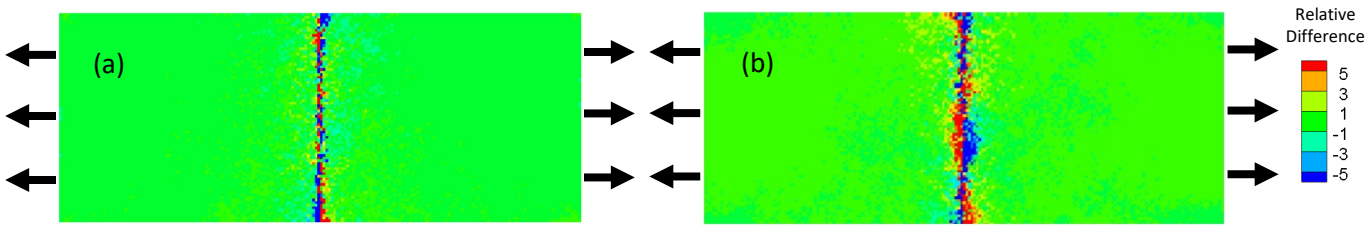

Fig. 5. The relative difference in horizontal displacements between the IH-PD solution and the analytical solution the classical model for a simple tension test (a) composite II, (b) composite I with the calibration discussed in section 4.2.I.

To compare, qualitatively, the stress computed with the IH-PD model versus that from a classical model, we also create a FE solution of a classical model for a typical transverse cross-section of a unidirectional FRC with a detailed microstructure and the fiber volume fraction of 35%. We consider the FE model with the same size and boundary conditions as in Fig. 5. A comparison of σ_{xx} between ANSYS and the IH-PD model is shown in Fig. 6. Both models show high stresses distributed throughout the FRC. The computation of stress components from PD results is performed as a post-processing step, as described in Appendix C.

Note that while the IH-PD model will not capture the fine details a model with explicit geometry does, it still maintains the intrinsic small-scale variability of stresses that would otherwise be fully smeared out with a fully homogenized model. This has important consequences in using the model in fracture and failure problems, since crack initiation and propagation is determined by such local variations in stress/strain fields [53]. The partial homogenization in the IH-PD model is a computationally inexpensive way to maintain such features without the need of the explicit geometry of the microstructure. Note that the explicit geometry solution with ANSYS uses a much finer mesh, to conform to the fine-scale of the fibers cross-section geometry. The FEM solution in Fig. 6.a used 67k nodes, while the IH-PD solution used 16k.

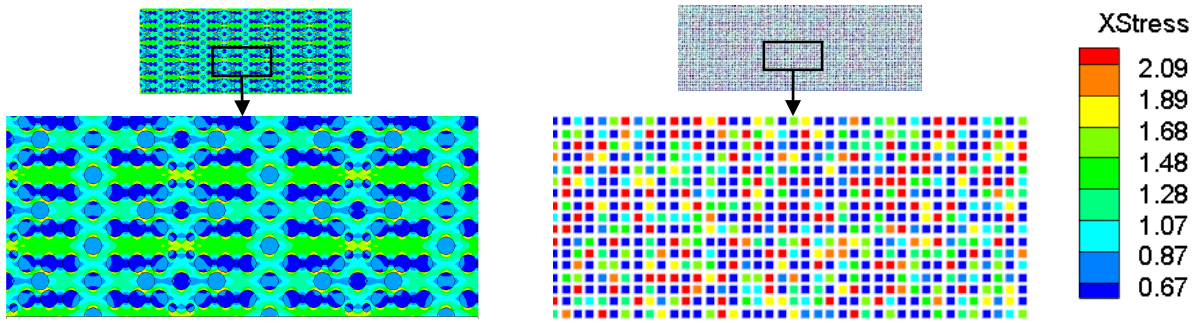

Fig. 6. A qualitative comparison of σ_{xx} between a typical transverse cross-section of a unidirectional composite with f=35% modeled explicitly in ANSYS (a), and its corresponding IH-PD model (b). Units in the color bar are MPa.

In this section, we verified the elasticity obtained by IH-PD model via a simple tension test. This may not be sufficient, since in other deformation modes, the influence of the specific connectivity of the fiber-phase, for example, may play a significant role. Since the partial homogenization scheme in the IH-PD

model does not take into account the specific topology of the composite phases, the model's behavior might not be the expected one in, for example, a bending-type deformation. In the next section, we test the elastic response of the IH-PD model under bending.

4.2. Verification and calibration for elastic behavior under three-point bending test

Here we consider the elastic response for the IH-PD model under three-point bending conditions for the transverse cross-section of a unidirectional FRC. To see if the contrast between the elastic moduli of the two phases or their volume fractions influences the results, we test both composites I and II (see Table I for material properties). We use displacement-controlled transverse loading with the boundary conditions shown in Fig. 7a.

Applying the imposed displacement at one node only, introduces a significant peridynamic surface effect (see [45]). For this reason, point-loadings need to be distributed over a certain area. On the other hand, if the area where displacements are enforced is large, the response in that region will be affected because nodes subjected to the same displacements move together and, therefore, generate zero force between them. To limit these issues and their effects on the solution, we apply the imposed loading displacements and the support constraints over two-node by two-node regions. The length of our computational sample is the same (the span between the supports used in the experiments). With a decreasing grid spacing, the effective modelled length between supports increases slightly, becoming closer to the span used in the experiments.

Since experimental data is provided in terms of load versus crack mouth opening displacement (CMOD), we obtain the external force equivalent to the applied displacement by summing up, after each displacement increment, the PD pairwise forces at nodes where displacement is imposed.

I. Case of the composite with a large elasticity contrast between phases (Composite I)

The sample used in [21] had a cross section 2.8mm (D)×2.0mm (t) and a loading span (S) of 11.2 mm [21]. The initial notch is cut with a tip radius of 130 μm and a length (a_0) of 0.5D (see Fig. 7.a). The loading direction is transverse to fibers, with a loading speed of 100 μm/min. Material properties for this FRC sample are listed in Table I. The ratio between the fibers and matrix elastic moduli is about 22 to 1, and fiber fraction is 54%. The load vs. crack mouth opening displacement (P-CMOD) data measured in this experiment, from five different tests, is shown in Fig. 7.b.

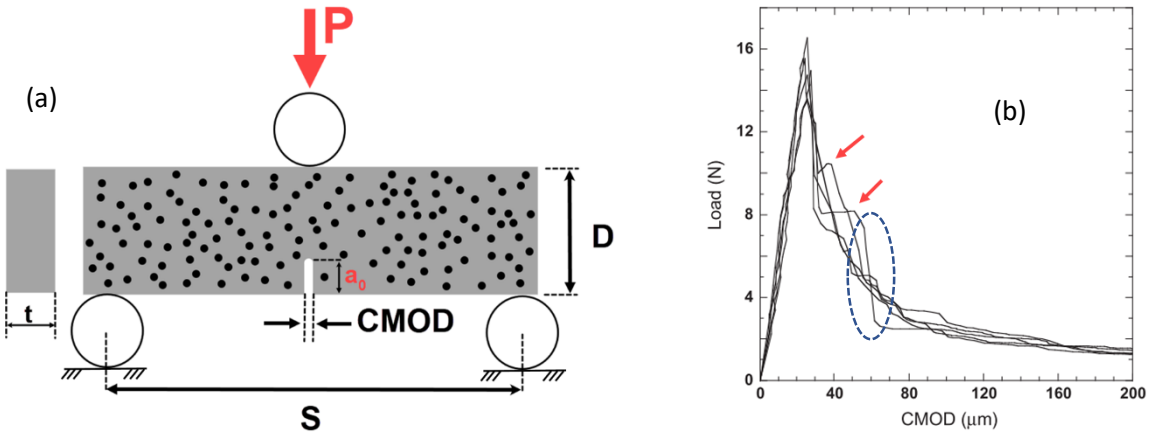

Fig. 7. (a) FRC sample geometry and experimental setup, and (b) the P-CMOD curve of the fractured tests (from [21]).

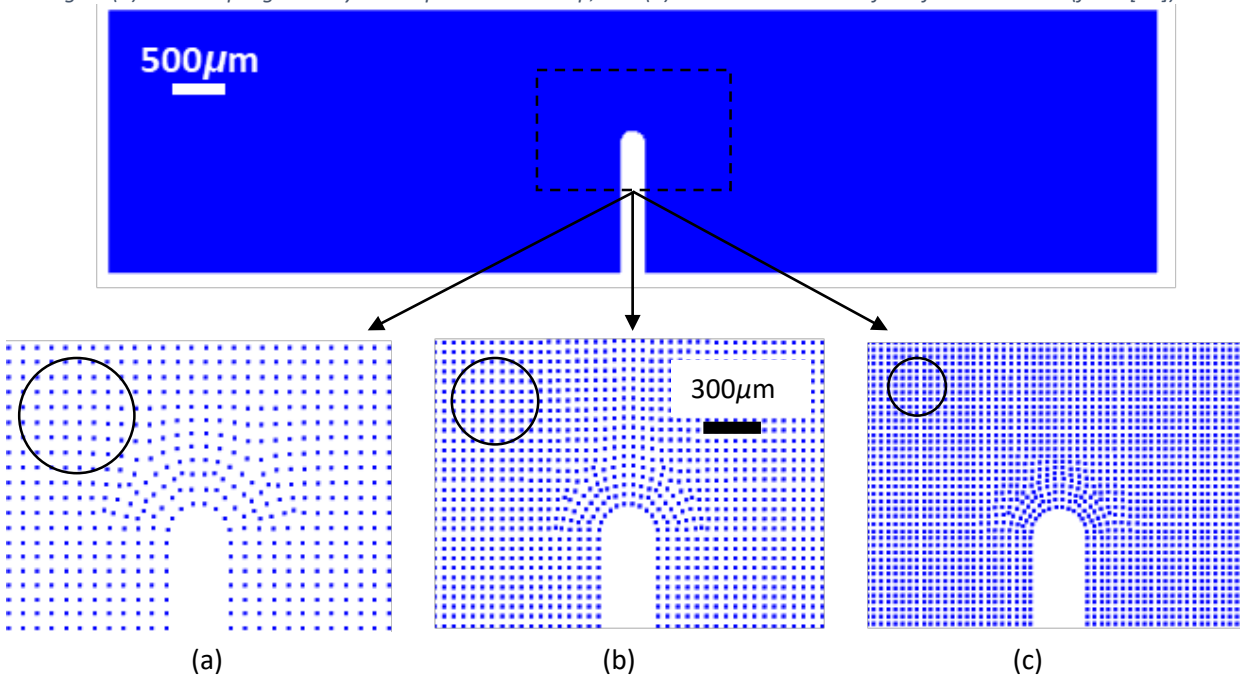

Fig. 8. Magnified views for PD model non-uniform, conforming grids around the notch for (a) δ=300 μm, (b) δ=225 μm, and (c) δ =150 μm. The horizon size is shown with a circle.

We perform a δ-convergence study for the elastic behavior in bending of the sample with the notch (see [32]). To simulate the three-point bending test using the IH-PD model, and perform the δ-convergence study (in terms of the horizon size while keeping the number of nodes covered by a node's horizon roughly the same), we create non-uniform meshes (since these conform better to the round notch tip) with three different element sizes of 75, 56, and 37.5 μm (corresponding to horizon sizes of 300, 225, and 150 μm respectively) (see Fig. 8 and Appendix B). Since the IH-PD model's microstructure is stochastic, each time we run the simulation we get a slightly different result. Results from three different runs with δ = 150 μm are overlapping over the elastic response region (see Fig. 9.a). This demonstrates that the stochasticity in the model does not affect its elastic behavior much, if at all, even if the local stiffness around the tip of the notch mouth may vary slightly between different runs. This is because the horizon

size in these runs is at the scale of the characteristic length of the notch size. The convergence shown in Fig. 9.b indicates that the material response converges as horizon decreases. In Fig. 9 (and through the rest of the paper) the elastic part of the response from the five experimental tests is shown as one shaded region.

Using Equation 11 and material properties in Table I, a value for E_{Tsai} of 12 GPa is approximated for the FH-PD model. The result with the FH-PD model is shown in Fig. 9.a. The computed elastic response falls within the experimental range, due to the Halpin-Tsai homogenization rule used.

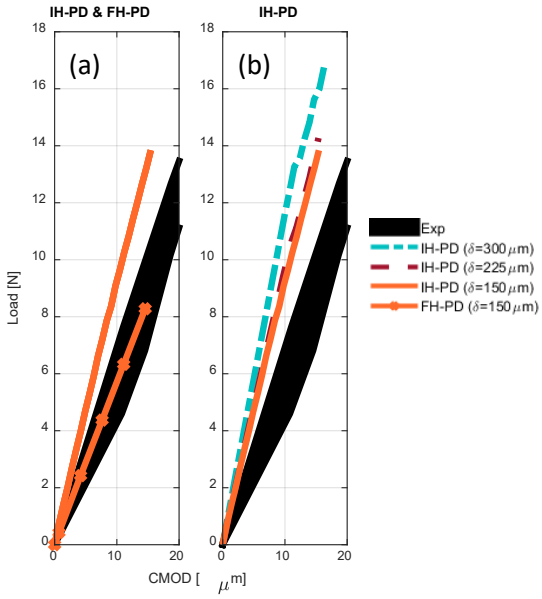

Fig. 9. Comparison of elastic response between PD models and experiments (from [21]): (a) P-CMODs of three IH-PD and one FH-PD simulations with δ = 150 μm; (b) δ-convergence study for IH-PD model.

The stiffer response obtained by the IH-PD model compared with the experiments is visible. This difference is likely due to differences in topology between the transverse cross-section of the FRC (in which the fiber phase is disconnected) and the IH-PD model in which the phases are interpenetrating, thus the fiber-bonds, for example, connect from one end to the other. This difference did not influence the tensile behavior, as we saw in the previous section, but the bending behavior is clearly affected. One way to resolve this issue, while still using only the minimal information about the phases volume fraction in the IH-PD formulation, is to calibrate the elasticity obtained by IH-PD model (see below, Equation 13) to the transverse modulus derived in the Halpin Tsai equation (Equation 11). Therefore, we enforce the condition:

$$E_{IH} = f^2 E_f + (1-f)^2 E_m + (1 - f^2 - (1-f)^2) E_{intf} = E_{Tsai} \tag{13}$$

where E_{IH} is the composite elastic modulus from the IH-PD model based on the combination of parallel bonds with properties of E_f, E_m, and E_{int}. From this equation, we can either compute a new, calibrated

fiber-bond modulus E_{f-IH} (Case A) or compute a new, calibrated fiber volume-fraction f_{IH} (Case B), as follows:

$$E_{f-IH}/E_m = \left(\frac{4(f^2-f)E_f/E_m}{1+E_f/E_m} + \frac{1+\xi\eta f}{1-\eta f} - (1-f)^2\right)/f^2 \tag{14}$$

$$(E_f + E_m - 2E_{int})f_{IH}^2 + 2(E_{int} - E_m)f_{IH} + (1 - \frac{1+\xi\eta f}{1-\eta f})E_m = 0 \tag{15}$$

where η and ξ are from Equation 11. By solving Equation 15 for f_{IH}, we obtain real roots, and at least one of them positive, as long as $E_m \leq E_f$, which is a reasonable assumption for this type of FRCs. In Fig. 10 we show the influence of E_f/E_m and f on E_{f-IH}/E_m. Note that when $E_f/E_m \leq 5$, the original IH-PD gives a very close value to E_{Tsai} and therefore E_{f-IH} is very close to E_f. In such cases, no calibration is required and the original IH-PD model can be used. This is also a reason why the IH-PD model gives the correct elasticity for composite II under unidirectional tensile loading (see section 4.1).

One can also calibrate values for parameters like E_m or E_{intf} instead of the fiber-bond elasticity or the fiber volume fraction. In what follows, we pursue solving Equation 14 or Equation 15 (under condition that the roots are real) to calibrate the IH-PD model.

For the composite I material properties we find the calibrated $E_{f-IH} = 28.7$GPa, and $f_{IH} = 0.327$ from Equations 14 and 15, respectively. A comparison of P-CMOD for models with the **same** random microstructure generated by the IH-PD model, for $\delta = 150\mu$m, and with the above corrections (Case A calibrating the elasticity of fiber bonds, Case B calibrating the fiber volume fraction), is shown in Fig. 11.a. The elastic response of the composite with calibrated material data for the IH-PD model are now within the experimental range, but somewhat on the lower part of the experimental observations, which would lead to a strength value lower than that shown in most tests reported.

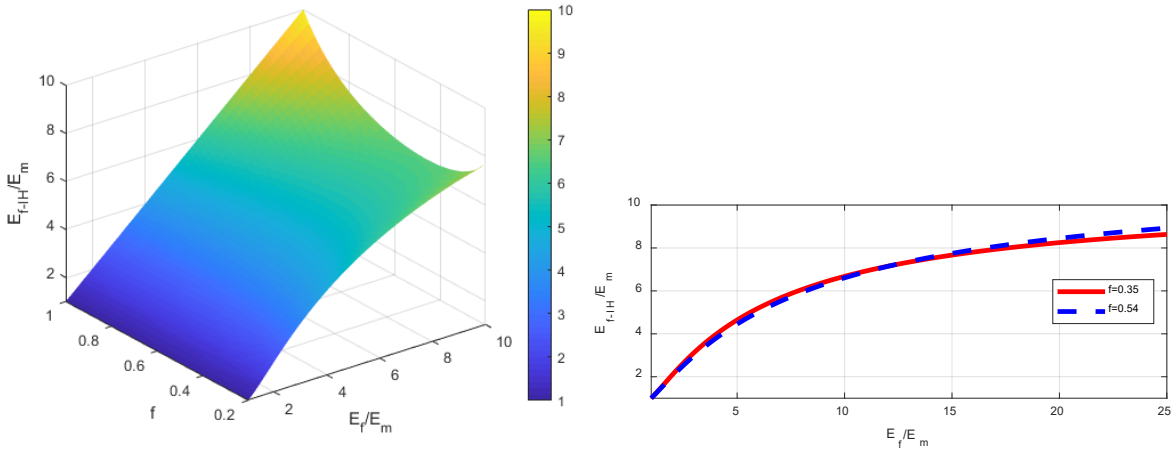

Fig. 10. Surface plot of calibrated fiber bond-modulus as a function of fiber volume fraction and the actual contrast between the fiber and matrix material elastic modulus (left plot). The particular dependency for $f = 35\%$ and 54%. Notice the nearly linear behavior values up to E_f/E_m<5 (right plot).

Since in this type of bending deformation with a pre-notch the behavior is controlled, to a large extent, by the properties near the tip of the notch, and being aware of the peridynamic surface effect ([45]), it is of interest to also provide results in which surface corrections strategies are used. In PD, material near the boundary behaves slightly softer than material in the bulk (which is used to compute the bond properties) due to the incomplete horizon region at these nodes. To reduce the surface effect, we use the method described in [45] and referred to as the surface correction with the volume method. We increase the micromodulus of bonds (Equation 7) based on the stiffening factor λ formulated as:

$$\lambda = \frac{2V_0}{V_x + V_{\hat{x}}} \tag{16}$$

where V_0 is the full horizon volume ($\pi\delta^2$ in 2D and $\frac{4}{3}\pi\delta^3$ in 3D), V_x and $V_{\hat{x}}$ are the *neighbor volumes* of nodes x and $\hat{x}$, respectively (see [45] for details). With the surface correction, a stiffer elastic behavior is obtained by the IH-PD model in both cases A and B (see Fig. 11.b), with the response for Case A sitting at the average response measured in experiments.

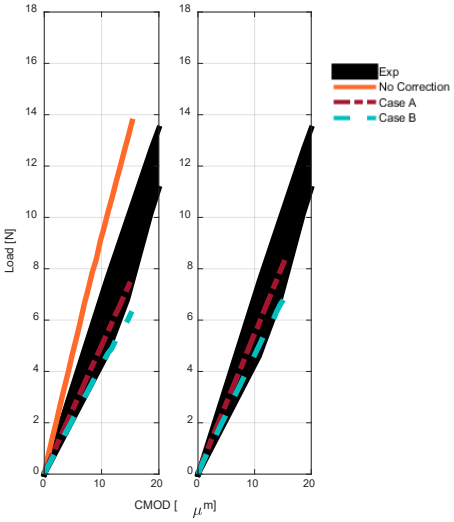

Fig. 11. Comparison of the IH-PD model against experiments (black-shaded area, from [21]) for the elastic behavior of transversely loaded unidirectional FRC in three-point bending. Left: P-CMODs from IH-PD simulations with δ = 150 μm without calibration, for cases A (calibrated fiber-bond modulus) and B (calibrated fiber-bond volume fraction); Right: same as in the Left graph but with the peridynamic surface correction.

We also perform δ-convergence studies for the calibrated IH-PD model (both cases A and B) with the peridynamic surface correction applied. The results are given in Fig. 12, along those from the experiments.

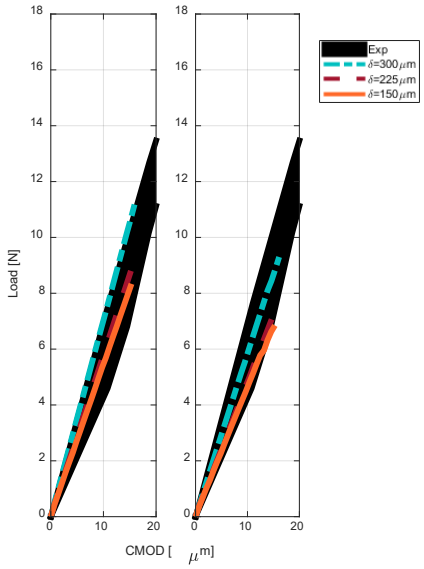

Fig. 12.The δ-convergence for load versus crack-mouth opening displacement for the calibrated IH-PD model, with PD surface correction for case A (left figure) calibrated E_{f-IH}, and case B (right figure) calibrated fiber volume fraction, f_{IH}.

We also test if this calibration for bending deformation compromises the results under the simple tension test. For this, we use the case A calibration with surface correction, in the simple tension test from Section 4.1. The results, comparing the IH-PD solution with the classical model, are shown in Fig. 5.b. We observe a minor influence of the calibration under bending deformation test on the tensile deformation response.

II. Case of the composite with a small elasticity contrast between phases (Composite II)

We test the robustness of the calibrated IH-PD model by now using a composite system with a different fiber volume fraction value and a different contrast of fiber to matrix Young's moduli. Material properties for this composite II (see Table I) under three-point bending loading conditions at ambient temperature are given in [51]. The dimensions of the specimen were *S*=30 mm, *D*=8 mm, *t*=1.35 mm, and a_0=0.2D, with a notch tip radius of 75 µm. To simulate the presence of the notch, we remove nodes inside the notch and break all bonds crossing the notch region. For this composite, the horizon size of 0.4 with m-factor of 4 is used. For the FH-PD model, as described in section 4.1, we obtain an elastic stiffness of 164 GPa for the transverse modulus. With the IH-PD model, for this composite, the E_f/E_m is less than 5, which means that the difference between E_f and the calibrated E_{f-IH} is small. Therefore, we do not use the calibration in this case.

Fracture of titanium reinforced with SiC fibers shows intense plastic deformations before failure, localized at matrix near the crack tip [51, 54]. Since the models employed here perform only elastic deformations and brittle-like failure, we only compare the elastic part of the response with the experimental data from [51] (see Fig. 13). Both the FH-PD and IH-PD models give a linear response under three-point bending deformation that matches well the experiments. Different realizations of the IH-PD microstructure lead

to essentially the same response as that shown in (Fig. 13). The FH-PD model (based on Halpin-Tsai homogenization) gives a slightly stiffer response in this case, while in the composite I case (Fig. 9.a) it was in the range of the experimental values. This difference could be attributed to the different contrast between the matrix/fiber stiffness in the two examples.

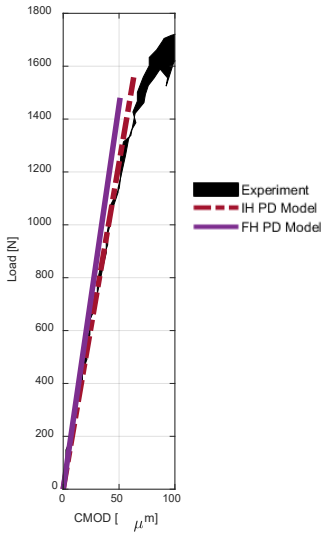

Fig. 13. Comparison of load vs. COMD for composite II between experimental data and the FH-PD and IH-PD models results. Computed results obtained with δ=400 μm. Experimental data from [51].

In conclusion, the IH-PD model calibrated to match the transverse modulus obtained by the Halpin-Tsai equation matches well the measured elastic behavior of transversely loaded unidirectional FRCs, for different fiber fractions (here f=54% and 35%). Note that, this calibration is only necessary for the IH-PD model when the contrast in the elastic moduli (E_f/E_m) is higher than five. The FH-PD model uses the transverse modulus obtained by Halpin Tsai equation directly.

5. Fracture in transversely-loaded fiber-reinforced composites

5.1. Results from experiments in [21]

We now study intraply fracture of the fiber-reinforced composite described in Section 4.2I. As can be seen from the experimental results in Fig. 7.b, before the peak load ($P_{max} \cong$ 12.5-16.5 N), the P-CMOD curves are approximately linear followed by an abrupt and then milder drop. The cracks appear to initiate along the fiber-matrix interfaces, and with further deformation, they merge into longer cracks that connect into a main crack starting at the pre-notch tip (see Fig. 14). It can be noticed in the experimental results that the load does not drop monotonically. In several instances the load reaches a "plateau" as the crack mouth continues to open: the load can stay relatively constant for a while, or even briefly increase (see Fig. 7.b). As the imposed displacements at the loading point continue to increase, the mouth opens more and the load eventually drops to near zero values. The sample is not fully broken at the end of the test data shown in Fig. 14. The SEM images from [21] shown in Fig. 14 are taken near the pre-notch tip

when CMOD is 45 and 53 µm, respectively. The crack path tortuosity appears to span a width similar to that of the pre-notch.

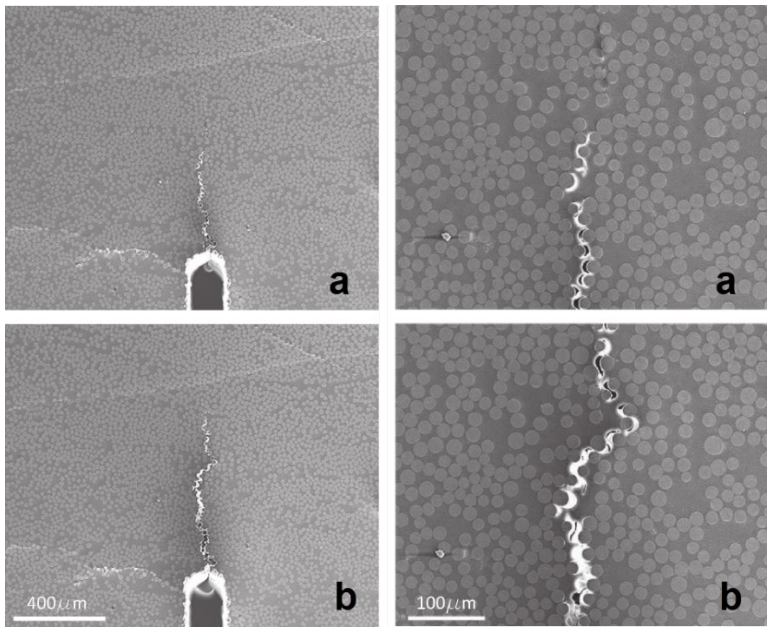

Fig. 14. SEM images of crack propagation from the tip of the pre-notch, taken at (a) CMOD =45 µm, and (b) at CMOD = 53 µm (from [21]).

5.2. PD models for the fracture problem

In this section we setup the PD models to simulate the fracture of the composite described in Section 4.2I. For a δ-convergence study, we select horizons of 300, 225, and 150 µm (with *m*-factor value of 4), with the smallest one being close to the size of the smallest geometrical feature in the sample (in this case the pre-notch width, or tip radius, see [55]). For PD models with a horizon size larger than the pre-notch width (*t*=260 µm), a pre-crack is defined in the middle of pre-notch by breaking all bonds crossing the pre-notch mid-line, as a pre-processing step.

Since the critical fracture energy for this composite is not available experimentally, we assume a value of 150 Jm^{-2} for the FH-PD model (the same as the value used in the modeling part of reference [21]). For the IH-PD model we use the fracture energy listed in Table I, where the interface fracture energy is assumed to be equal to that of the matrix. In the transverse loading of a unidirectional FRC, fibers do not break. Our IH-PD model creates a random distribution of fiber, matrix, and interface type bonds selected to match the volume fraction of the two composite phases. When the fiber volume fraction in the FRC is 54%, nearly 29% of the PD bonds created by the IH-PD model that connect to a PD node are assigned as fiber-fiber (F-F) bonds (see Section 3.2). Due to this, continuous chains of F-F bonds may exist in the IH-PD material structure of the transverse cross-section of the unidirectional FRC (in which the fiber phase is disconnected). Under bending, such chains would not likely break if we assign them a critical strain matching the critical fracture energy of the fiber material. This would prevent us from correctly

representing the actual failure mechanism in the sample, which is solely controlled by matrix and fiber-matrix interface cracks/damage, since the fiber phase is disconnected. To overcome this problem, we set the critical fracture energy of 150 Jm^{-2} for the PD fiber-bonds in the IH-PD model (same as for the interface bonds, and the same with the value used in [21]).

We also implement the damage-dependent material model in the PD models (see [56, 57]). This effectively reduces the PD surface effect in terms of strength for areas that are suffering damage. The modified critical bond strain, depending on the amount of damage at a node, is:

$$s = \begin{cases} s_0 \times \min\left(\gamma, 1 + \beta \times \dfrac{D-\alpha}{1-D}\right), & D > \alpha \\ s_0, & \text{Otherwise} \end{cases} \tag{17}$$

where the damage index D is defined as the ratio of the number of broken bonds to the number of bonds at a node; s_0 is the critical bond strain (computed for a node in the pristine bulk) ; parameters α, β, and γ are damage stretch coefficients, and the values $\alpha = \beta = 0.2$ and $\gamma = 1.4$ are used here. When $\alpha = \beta = 0$ and $\gamma = 1$, we recover the constant s_0 model.

We noticed that in order to fully split the sample, we needed to apply a total imposed displacement of about 250 μm. The CMOD at full failure is also larger than 250 μm. The range of data reported in the experiments from [21] (see Fig. 7.b) stops at a CMOD value of 200 μm. Because of this, we will only show P-CMOD data computed by our models over the same range as that provided in the experimental data. We, however, show the crack paths at full sample fracture.

The algorithm for quasi-static fracture is as follows: the equilibrium equations are solved using the NCG method (see section 4) for the current imposed boundary conditions, and the potential bonds to break are found. If no bonds reach their critical strain, the next increment of displacement is applied. Otherwise, after bonds are broken, the NCG solver is called again (without a new displacement increment). In quasi-static crack growth, the displacement increment needs to be chosen so that not too many bonds break at each increment, otherwise crack growth becomes unstable [58]. In our example, an increment of 1μm in the imposed displacements satisfies this condition.

The experimental data is shown in terms of reaction force at the point of application of the loading versus CMOD. We compute the reaction force value as follows: we consider the nodes were the incremental displacements are imposed; we sum up the nodal forces (as vectors) over these nodes to obtain the total reaction load *P* (by using the magnitude of the vertical component of the total force), before applying next displacement increment. Since our 2D PD model is under plane stress conditions and per unit thickness, we multiply the load by the thickness of the sample (to obtain the equivalent 3D load as in the experiment).

6. Numerical results for three-point bending fracture tests

We use both the damage-dependent FH-PD and IH-PD (calibrated and before calibration) models to compute the load-versus CMOD and crack paths for the three-point bending test of the transversely loaded unidirectional FRC (composite I). Results are compared with those from the experimental tests conducted in [21].

The δ-convergence results from the FH-PD model are given in Fig. 15.a. The experimental data extracted from Fig. 8.b is shown as an aggregate (the black-shaded area), pointing to the spread of results from five different experimental samples. The composite's material variability leads to a range of stiffness values in the elastic response for the three-point bending experimental tests (see Fig. 8.b). Moreover, the failure behavior also has a significant "spread" between the several samples tested in [21], also caused by variations in the material.

In the numerical modeling of a three-point bending test with a pre-notch, the computed elastic response is especially influenced by the accuracy near the notch tip. In the FH-PD model, slight variations in the elastic response are seen as the horizon changes (see Fig. 15.a). Once the nonlocal size is in the scale of the tip radius, the stress profile is near that of a classical elasticity model, and convergence is achieved. Observe that the failure behavior also converges. Non-uniform grids around the tip of the notch are useful since they can conform better to round shapes and lead to more accurate stress profiles near stress-concentration zones, and therefore, an improved failure behavior (see [44]).

Analyzing the results with the FH-PD model in Fig. 15.a, we find that the FH-PD model is able to reproduce the main characteristics of the failure process: an elastic part reaching a peak load, followed by a rapid drop in load and eventually a more gradual decrease in load versus CMOD. However, the FH-PD model fails to reproduce some of the details in the load-versus-CMOD behavior (the load "plateaus", between sudden load drops, for example), and shows no crack tortuosity. Experimental results for the early part of the crack growth process shown in [21] and reproduced in Fig. 14, show a tortuosity in the same scale as the width of the pre-notch.

The computed peak load matches the experimental range. Once the horizon size is similar to the size of notch width, the results change little between different horizon values. In the plateauing region beyond a CMOD of 100 μm, the computed results with the FH-PD model tend to slightly underestimate the experimental observations. Damage maps showing the crack path at full splitting of the computational sample are shown as insets in Fig. 15.b, for horizon sizes of 225 and 150 μm. Regardless of the horizon size, the crack initiates at the tip of the notch and propagates straight in all of the FH-PD models.

Due to their inherent stochasticity in assigning bond-properties (see Section 3.2), IH-PD models lead to slightly different results even when using the same horizon size and grid, as seen in Fig. 16.b, c, and d, where three different runs (with the random number generator reset for each run) use the same horizon size and computational grid. In Fig. 16.a we present the results obtained from two different realizations of the material microstructure as a band in the P-CMOD graph (see Fig. 16.a), for each of the horizons

tried. Stochasticity of the IH-PD model leads to crack tortuosity, similar to the actual behavior of the fracture process, regardless of the horizon size. Sudden drops in load versus CMOD curves are observed in the experiment (see elliptical dash area in Fig. 7.b). This behavior is also noticeable in all IH-PD model results, for each horizon size (see Fig. 16), but not in the FH-PD model with the smaller horizons (see Fig. 15). The variability in bond properties in the IH-PD model is responsible for this behavior. The δ-convergence trend is noted for the entire elastic-and-failure behavior of the system.

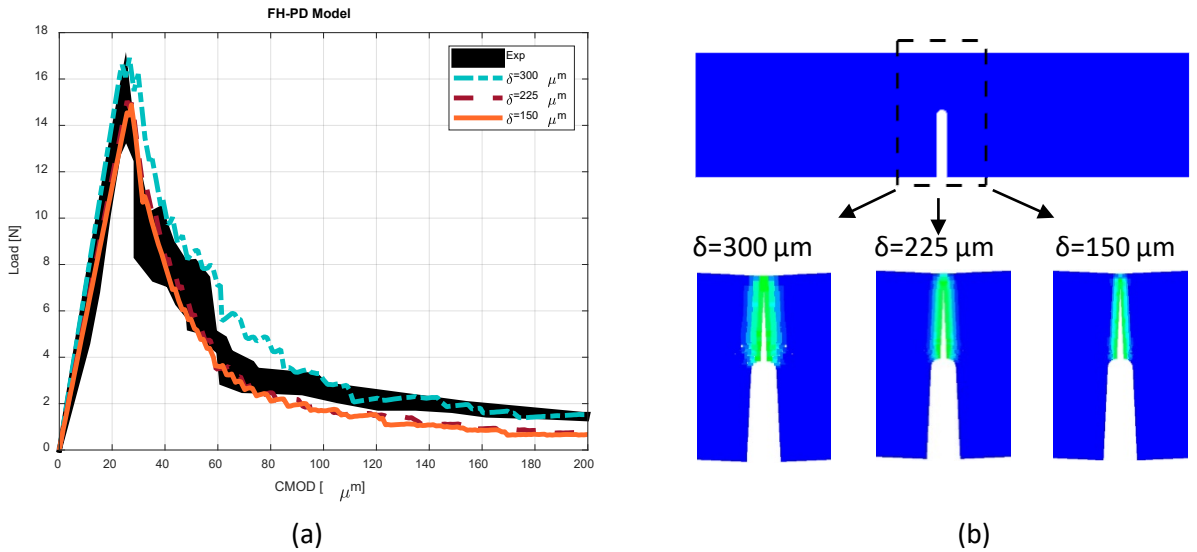

Fig. 15. Results with the FH -PD model (a) δ-convergence study comparing the load versus crack mouth opening displacement from the experiments in [21] with those from the FH-PD model (b) Damage maps for different horizon sizes show straight crack propagation. Damage maps are shown at full failure, when CMODs are beyond 250 μm.

Comparing the load-versus-crack-mouth-opening-displacements from the FH-PD and IH-PD models with experiments, we can conclude that both models perform well. Some differences between the models' results can, however, be noted:

1. The microstructure heterogeneity in the IH model drives the crack path tortuosity, which is maintained even as the horizon decreases. This was not the case for the FH model. Crack tortuosity is observed in experiments (see Fig. 7.b).
2. The secondary peaks in the P-CMOD plots (caused by the increased level of force needed to further open the crack mouth after a certain increase in crack length) seen from the IH-PD results resemble the experimental data, while the results obtained with the FH-PD model converge (as the horizon decreases) to a monotonous response. This is due to the heterogeneity present in the IH-PD model, which mimics the actual heterogeneity (only in terms of volume fraction), but does not use the detailed microstructure geometry.

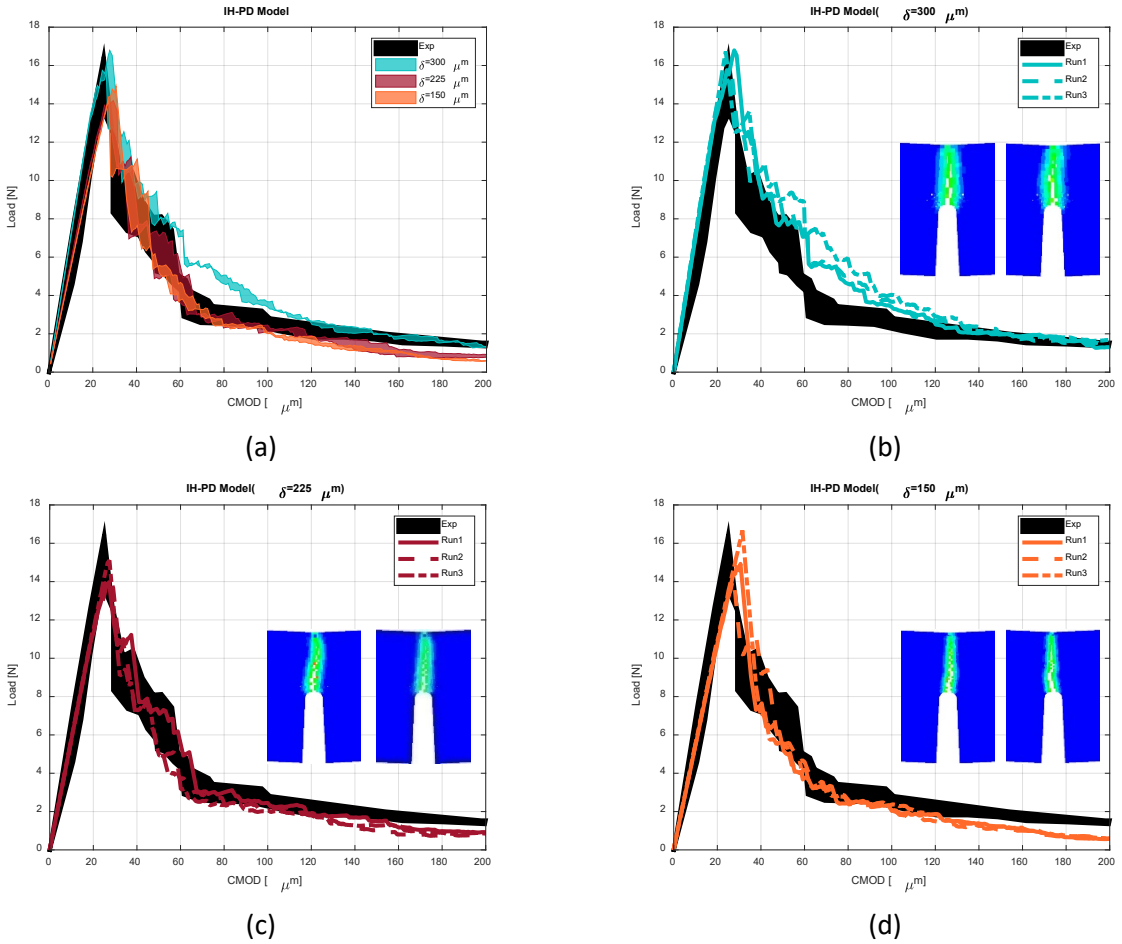

Fig. 16. Load versus CMOD: comparison between experimental results (from [21]) and those computed with the calibrated IH-PD model: (a) δ-convergence results; three different runs with different microstructure realizations for δ=300 μm (b), δ=225 μm (c), and δ=150 μm (d).

To observe the overall influence of the calibration and surface corrections for the IH-PD model in this transverse failure of a unidirectional FRC, we present results from using the IH-PD model without surface correction and without the calibration of the fiber-phase modulus (see Section 4) in Fig. 17, with three horizon sizes: $\delta = 300, 225$, and 150 μm. As discussed in section 4, the original IH-PD model (without the calibration to account for the topology of the phases) gives a stiffer response for the elastic region. A higher stiffness leads to higher strength (peaks in loading) compared with the experiment. However, as can be seen from Fig. 17, the failure behavior produced by the original IH-PD model follows closely what is observed experimentally. Here we used similar fracture energies in all IH-PD simulation (with or without calibration). We can conclude that the IH-PD model, independent of whether calibration is employed, correctly captures the failure mode (at least in terms of its force-versus-CMOD behavior). Note that crack tortuosity and sudden drops and partial recovery in the load-CMOD curves are also observed in all IH-PD simulations.

It is interesting to observe that all of the simulation results for the P-CMOD behavior, whether obtained with the FH-PD model or the IH-PD models, underestimate the reaction force when the CMOD is above

100-120 μm value. This is likely due to the surface effect along the growing crack surfaces. The only surface correction we used here was on the boundaries of the sample in its initial state, most importantly around the pre-notch tip.

All runs were performed with a CUDA C code implemented for a single CPU and a single GPU [59]. The FH-PD and IH-PD simulations using the smallest horizon (150 µm) and finest grids, over 250 load-steps, take about four hours to complete on an Intel Xeon E5-2670 2.60GHz processor with the Tesla P100 GPU.

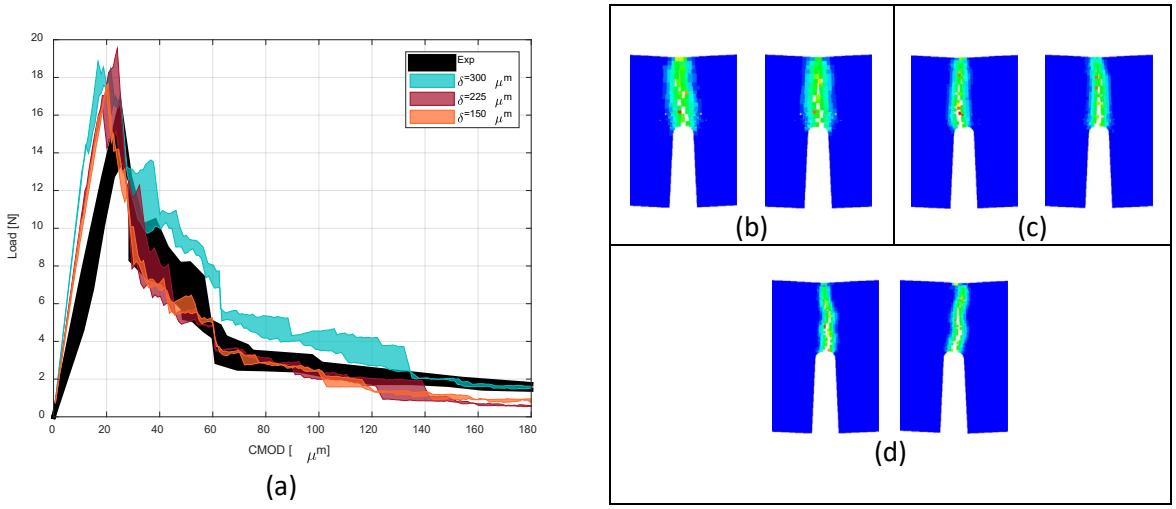

Fig. 17. Load versus CMOD: comparison between experimental results (from [21]) and those computed with the IH-PD model without the surface correction and the calibration for fiber-bonds' elasticity: (a) δ-convergence results; damage maps for two different runs with different microstructure realizations for δ=300 µm (b), δ=225 µm (c), and δ=150 µm (d).

7. A case with different fracture pattern between the FH-PD and IH-PD models

While for the three-point bending cases shown in the previous cases, both the FH and IH-PD models perform well (with a slight advantage for the IH model), we now investigate a potential loading configuration in which the two models give dramatically different results. This example is motivated by the study on porous rock performed in [32] on a three-point bending sample with an asymmetric notch. In [32] it was shown that only an IH-PD type model (applied for a porous and elastic material) is able to replicate experimental observations in which the crack initiation point depends on the length of the pre-notch.

With the IH-PD model for the two-phase composite in the current paper, we investigate a similar configuration as the one analyzed in [32]. The transversely-loaded FRC we consider here is the one described in section 4.2I. The cross section is 2.8mm (D)×2.0mm (t) and the loading span (S) is 11.2 mm. The initial notch has a tip radius of 130 µm and a length (a_0) of 0.2D. Here, instead of varying the notch length, we vary its location, placing it closer and closer to one of the ends. We then run both the FH-PD and IH-PD models and notice the failure patterns. When the notch is placed at a distance of 4.5 mm from the center, we notice (see Fig. 18) that the IH-PD model predicts the crack to grow from near the center of the sample, instead of the tip of the notch. The FH-PD model gives a crack that grows from the notch

tip, independent of the placement of the notch. For these results we used a horizon size of δ =225 μm and the same non-uniform mesh with global element size of 55 μm.

We show these results as an invitation to experimentalists to try such configurations and loading conditions, as a test for our computational models.

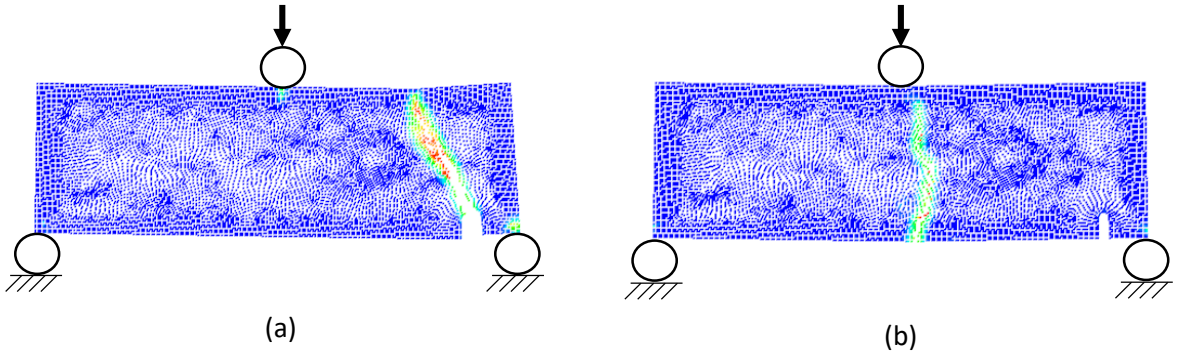

Fig. 18. The damage maps showing different failure patterns from three-point bending of transversely-loaded unidirectional FRCs with a pre-notch near the end of the sample obtained with the (a) FH-PD model and the (b) IH-PD model.

8. Conclusions

The intermediately homogenized peridynamic (IH-PD) model, in which a stochastic microstructure is created to match the fiber volume fraction in the composite, was introduced to study the transverse fracture behavior of unidirectional fiber-reinforced composites (FRCs). Results from this model for fracture induced by three-point bending were compared with experimental data from the literature and with data from a fully homogenized peridynamic model (FH-PD) approach based on the Halpin-Tsai formula for transverse loading. We verified the IH-PD model for a simple tension test and observed that, while the model does not utilize the microstructure geometry of the FRC, it induces heterogeneous stresses that resemble stress variations in a model that uses the explicit geometry. The computational cost of the IH-PD model is, however, similar to that of the FH-PD model.

Noting that the IH-PD model does not take into account the topology of the composite phases (in this case the discontinuous fiber phase in the transverse FRC direction), we found the elastic response for bending in the transverse direction of the unidirectional FRC to be stiffer than the real one. To overcome this, we proposed a calibration to the modulus given by a Halpin-Tsai model for the transverse direction. With this calibration, needed especially when the contrast between the Young's moduli of the two phases is high, the IH-PD model converges, as the nonlocal region decreases, to the measured response in three-point bending tests.

We simulated the three-point bending fracture in a $[0]_{14}$E-glass/MTM57 composite with the FH-PD and the IH-PD models using conforming discretization around the pre-notch tip. Once the nonlocal region size (the peridynamic horizon) was at the scale of the pre-notch tip, the peridynamic simulations with both the FH- and IH-PD models led to load-versus-crack mouth opening displacement (P-CMOD) curves that matched the experimental results well through full sample failure. However, only the IH-PD model gave a

non-monotonic load-crack-opening softening curve, similar to what is seen in experiments. Moreover, only the IH-PD models preserved the crack path tortuosity, also prominent in experiments.

The two models produced drastically different results in a three-point bending test with a notch located off-center. At some point, by placing the pre-notch closer to the end of the sample, the IH-PD model showed a crack path that did not start from the notch, but rather from the center of the beam. This was in stark contrast with the results from the FH-PD model where the fracture starts at the pre-notch, irrespective of the pre-notch location. Experiments to verify which model better represents reality are sought.

9. Acknowledgment

This work has been supported by AFOSR MURI Center for Materials Failure Prediction through Grant Number FA9550-14-1-0073 (program managers Drs. Jaimie Tiley, Ali Sayir, David Stargel, and Fariba Fahroo), and ONR Award #N00014-16-1-2173 (program manager William Nickerson). This work was completed utilizing the Holland Computing Center of the University of Nebraska, which receives support from the Nebraska Research Initiative.

Appendix A

This appendix describes the algorithm used for the nonlinear conjugate solver (CG). The CG solver is started with the steepest direction, and the secant method is used to search for the next point along the CG step. The stopping criterion used for the CG iterations and the line search are defined as

$$\delta_{new} > \epsilon_{CG}^2 \delta_0 \tag{18}$$

$$\alpha^2 \delta_d > \epsilon_{LS}^2 \tag{19}$$

where δ_{new} and δ_0 are dot product of the residual and the search direction, δ_d is the dot product of the search direction ($\boldsymbol{d}$), ϵ_{CG} is the NCG error tolerance, ϵ_{LS} is the line search error tolerance, and α is a coefficient, δ_0 is. The value of ϵ_{CG} and ϵ_{LS} is 10^{-5} which is sufficiently small for the utilized hybrid method that ensures no noticeable crack path differences when smaller convergence tolerance values are used. To improve the convergence rate, the efficient hybrid method proposed by Dai and Yuan is implemented in NCG by changing Polark-Ribiere β to β_k as follows [43].

$$\beta_k = \max\{0, \min\{\beta_k^{HS}, \beta_k^{DY}\}\} \tag{20}$$

$$\beta_k^{HS} = \frac{g_k T(g_k - g_{k-1})}{d_{k-1}^T (g_k - g_{k-1})}$$

$$\beta_k^{DY} = \frac{||g_k||^2}{d_{k-1}^T (g_k - g_{k-1})}$$

where

- HS: Hestenes–Stiefel
- DY: Dai-Yuan

- $g_k = -\nabla \mathrm{f}(\mathrm{x_k})$
- $d_k = \begin{cases} -g_k & \text{for } K = 1 \\ -g_k + \beta_k d_{k-1} & \text{for } K \geq 2 \end{cases}$
- k: iteration

The algorithm of the nonlinear conjugate gradient solver is shown below.

Algorithm 1 Nonlinear conjugate gradient solver

$i_{CG} = 0$
$i_{LS} = 0$
$i_{reset} = 0$
$\boldsymbol{r} = \boldsymbol{F}(\boldsymbol{u})$
$\boldsymbol{d} = \boldsymbol{r}$
$\boldsymbol{s} = \boldsymbol{r}$
$\sigma_0 = \frac{1}{E\Delta x}$
$\delta_{new} = \boldsymbol{r}^T \boldsymbol{r}$
$\boldsymbol{d}_{old} = \boldsymbol{r}$
while $i_{CG} < i_{CG,max}$ && $\delta_{new} > \epsilon_{CG}^2 \delta_0$
    $i_{LS} = 0$
    $\delta_d = \boldsymbol{d}^T \boldsymbol{d}$
    $\alpha = -\sigma_0$
    $\boldsymbol{u_t} = \boldsymbol{u} + \sigma_0 \boldsymbol{d}$
    $\eta_{prev} = [\boldsymbol{F}(\boldsymbol{u} + \sigma_0 \boldsymbol{d}]^T \boldsymbol{d}$
    Do
        $\eta = [\boldsymbol{F}(\boldsymbol{u})]^T \boldsymbol{d}$
        $\alpha = \alpha \frac{\eta}{\eta_{prev} - \eta}$
        $\boldsymbol{u} = \boldsymbol{u} + \alpha \boldsymbol{d}$
        $\eta_{prev} = \eta$
        $i_{LS} = i_{LS} + 1$
        while $i_{LS} < i_{LS,max}$ && $\alpha^2 \delta_d > \epsilon_{LS}^2$
    $\boldsymbol{r} = \boldsymbol{F}(\boldsymbol{u})$
    $\delta_{old} = \delta_{new}$
    $\delta_{new} = \boldsymbol{r}^T \boldsymbol{r}$
    $\delta_{mid} = \boldsymbol{r}^T \boldsymbol{s}$
    $\boldsymbol{s} = \boldsymbol{r}$
    $\beta_{HS} = \frac{\delta_{new} - \delta_{mid}}{\boldsymbol{d}_{old}^T (\boldsymbol{r} - \boldsymbol{s})}$
    $\beta_{DY} = \frac{\delta_{new}}{\boldsymbol{d}_{old}^T (\boldsymbol{r} - \boldsymbol{s})}$
    $\beta = \max\{0, \min(\beta_{HS}, \beta_{DY})\}$

31: $i_{reset} = i_{reset} + 1$
32: if $i_{reset} = n_{reset}$ or $\beta \leq 0$
33: $\boldsymbol{d} = \boldsymbol{r}$
34: $i_{reset} = 0$
35: $else$
36: $\boldsymbol{d} = \boldsymbol{r} + \beta \boldsymbol{d}$
37: $\boldsymbol{d}_{old} = \boldsymbol{d}$
38: $i_{CG} = i_{CG} + 1$

Appendix B

This appendix describes the APDL code used to find element centroids and areas and write them in an output file. A brief description is provided for each APDL line.

Table II ANSYS APDL code to generate PD nodes from element centroids

1:	*Get, eMax, Elem,, Count	! find total element number and set to eMAX
2:	*Dim, nodeID, array, eMax, 1, 1	! Create the nodeID array with size of eMAX
3:	*Vfill, nodeID, ramp, 1,1,	! Fill PD node list from 0 to eMAX
4:	*Vget, aear1, Elem,1, Geom, , ,2	! Create an array and fill it with element areas
5:	*Vget, xelem, Elem,1, Cent,X, , ,2	! Create two arrays and fill them with element
6:	*Vget, yelem, Elem,1, Cent, Y, , ,2	! Centroid position X and Y
7:	*Cfopen, 'nodal_data', 'txt',' '	! Create an output file
8:	*vwrite, 'nodeID xc yc vol'	! write PD nodes #, element centroid positions
9:	*VWRITE, nodeID(1), xelem(1), yelem(1), aear1(1)	! and element area to the output file
10:	(F10.0,3e16.6)	
11:	*cfclose	

Appendix C

This appendix describes the detail procedure to computed stresses in a 2D bond-based peridynamic simulation (see [60] for the state-based version of this).

Algorithm 2 for computing stresses in a 2D bond-based PD code at a generic node x_i

1:	$\boldsymbol{f}_i = \boldsymbol{0}$	% Total force on x_i
2:	$\boldsymbol{\sigma}_i = \boldsymbol{0}$	% Stress tensor at node x_i
3:	For all nodes $\boldsymbol{x}_j \in H_{\boldsymbol{x}_i}$	
4:	$\boldsymbol{\xi} = \boldsymbol{x}_j - \boldsymbol{x}_i$	
5:	$\boldsymbol{\eta} = \boldsymbol{u}_j - \boldsymbol{u}_i$	
6:	$s = \frac{\|\boldsymbol{\eta}+\boldsymbol{\xi}\| - \|\boldsymbol{\xi}\|}{\|\boldsymbol{\xi}\|}$	

7: $c = \frac{24E}{\pi\delta^3(1-\nu)}\left(1 - \frac{||\boldsymbol{\xi}||}{\delta}\right)$

8: $\boldsymbol{f}_i = \boldsymbol{f}_i + \frac{\boldsymbol{\eta}+\boldsymbol{\xi}}{\|\boldsymbol{\eta}+\boldsymbol{\xi}\|} c(\boldsymbol{\xi}) s V_j$

9: $\boldsymbol{\sigma}_i = \boldsymbol{\sigma}_i + \boldsymbol{f}_i \otimes \boldsymbol{\xi}$

10: End of loop for nodes $\boldsymbol{x}_j \in H_{\boldsymbol{x}_i}$

References

[1] E. Gamstedt, and B. Sjögren, "Micromechanisms in tension-compression fatigue of composite laminates containing transverse plies," *Compos Sci Technol.,* vol. 59, no. 2, pp. 167-178, 1999.

[2] P. Kanoute, D. P. Boso, J. L. Chaboche, and B. A. Schrefler, "Multiscale Methods for Composites: A Review," *Arch Comput Methods Eng.,* vol. 16, no. 1, pp. 31-75, 2009.

[3] R. Q. de Macedo, R. T. L. Ferreira, J. M. Guedes, and M. V. Donadon, "Intraply failure criterion for unidirectional fiber reinforced composites by means of asymptotic homogenization," *Compos Struct,* vol. 159, pp. 335-349, 2017.

[4] S. Nemat-Nasser, and M. Hori, *Micromechanics: overall properties of heterogeneous materials*, Vol. 37. Elsevier, 2013.

[5] S. Torquato, *Random heterogeneous materials: microstructure and macroscopic properties*, Vol. 16. Springer Science & Business Media, 2013.

[6] J. Llorca, C. Gonzalez, J. M. Molina-Aldareguia, J. Segurado, R. Seltzer, F. Sket *et al.*, "Multiscale modeling of composite materials: a roadmap towards virtual testing," *Adv Mater,* vol. 23, no. 44, pp. 5130-47, 2011.

[7] D. Y. Zhang, A. M. Waas, and C. F. Yen, "Progressive damage and failure response of hybrid 3D textile composites subjected to flexural loading, part II: Mechanics based multiscale computational modeling of progressive damage and failure," *Int J Solids Struct.,* vol. 75-76, pp. 321-335, 2015.

[8] C. Gonzalez, J. J. Vilatela, J. M. Molina-Aldareguia, C. S. Lopes, and J. LLorca, "Structural composites for multifunctional applications: Current challenges and future trends," *Prog Mater Sci.,* vol. 89, pp. 194-251, 2017.

[9] P. P. Castañeda, and P. Suquet, "Nonlinear Composites,"in *Adv Appl Mech*, E. van der Giessen and T. Y. Wu, eds., pp. 171-302: Elsevier, 1997.

[10] F. Naya, C. Gonzalez, C. S. Lopes, S. Van der Veen, and F. Pons, "Computational micromechanics of the transverse and shear behavior of unidirectional fiber reinforced polymers including environmental effects," *Compos Pt A Appl Sci Manuf.,* vol. 92, pp. 146-157, 2017.

[11] M. Herraez, D. Mora, F. Naya, C. S. Lopes, C. Gonzalez, and J. LLorca, "Transverse cracking of cross-ply laminates: A computational micromechanics perspective," *Compos Sci Technol.,* vol. 110, pp. 196-204, 2015.

[12] E. J. Pineda, B. A. Bednarcyk, A. M. Waas, and S. M. Arnold, "Progressive failure of a unidirectional fiber-reinforced composite using the method of cells: Discretization objective computational results," *Int J Solids Struct.,* vol. 50, no. 9, pp. 1203-1216, 2013.

[13] M. Herraez, C. Gonzalez, C. S. Lopes, R. G. de Villoria, J. LLorca, T. Varela *et al.*, "Computational micromechanics evaluation of the effect of fibre shape on the transverse strength of unidirectional composites: An approach to virtual materials design," *Compos Pt A Appl Sci Manuf.,* vol. 91, pp. 484-492, 2016.

[14] A. Arteiro, G. Catalanotti, A. R. Melro, P. Linde, and P. P. Camanho, “Micro-mechanical analysis of the effect of ply thickness on the transverse compressive strength of polymer composites,” *Compos Pt A Appl Sci Manuf.,* vol. 79, pp. 127-137, 2015.

[15] Q. P. Sun, Z. X. Meng, G. W. Zhou, S. P. Lin, H. T. Kang, S. Keten *et al.*, “Multi-scale computational analysis of unidirectional carbon fiber reinforced polymer composites under various loading conditions,” *Compos Struct,* vol. 196, pp. 30-43, 2018.

[16] K. Z. Rami, Y.-R. Kim, M. Khedmati, G. Nsengiyumva, and H. Alanazi, “Two-way linked multiscale method integrated with nanomechanical tests and cohesive zone fracture to model highly heterogeneous binding materials,” *J Eng Mech.,* vol. 144, no. 10, pp. 04018095, 2018.

[17] Y. Pan, L. Iorga, and A. A. Pelegri, “Numerical generation of a random chopped fiber composite RVE and its elastic properties,” *Compos Sci Technol.,* vol. 68, no. 13, pp. 2792-2798, 2008.

[18] I. Kaleel, M. Petrolo, A. Waas, and E. Carrera, “Micromechanical progressive failure analysis of fiber-reinforced composite using refined beam models,” *J Appl Mech.,* vol. 85, no. 2, pp. 021004, 2018.

[19] T. J. Vaughan, and C. T. McCarthy, “Micromechanical modelling of the transverse damage behaviour in fibre reinforced composites,” *Compos Sci Technol.,* vol. 71, no. 3, pp. 388-396, 2011.

[20] K. Z. Rami, S. Amelian, Y.-R. Kim, T. You, and D. N. Little, “Modeling the 3D fracture-associated behavior of viscoelastic asphalt mixtures using 2D microstructures,” *Eng Fract Mech,* vol. 182, pp. 86-99, 2017.

[21] L. P. Canal, C. Gonzalez, J. Segurado, and J. LLorca, “Intraply fracture of fiber-reinforced composites: Microscopic mechanisms and modeling,” *Compos Sci Technol.,* vol. 72, no. 11, pp. 1223-1232, 2012.

[22] P. F. Liu, and J. Y. Zheng, “Recent developments on damage modeling and finite element analysis for composite laminates: A review,” *Mater Des.,* vol. 31, no. 8, pp. 3825-3834, 2010.

[23] S. B. Biner, and S. Y. Hu, “Simulation of damage evolution in composites: A phase-field model,” *Acta Mater.,* vol. 57, no. 7, pp. 2088-2097, 2009.

[24] A. Yaghoobi, and M. G. Chorzepa, “Fracture analysis of fiber reinforced concrete structures in the micropolar peridynamic' analysis framework,” *Eng Fract Mech,* vol. 169, pp. 238-250, 2017.

[25] J. Mehrmashhadi, Y. Tang, X. Zhao, Z. Xu, J. J. Pan, Q. V. Le *et al.*, “The Effect of Solder Joint Microstructure on the Drop Test Failure—A Peridynamic Analysis,” *IEEE Trans Compon Packag Manuf Technol,* vol. 9, no. 1, pp. 58-71, 2019.

[26] S. Jafarzadeh, Z. G. Chen, and F. Bobaru, “Peridynamic Modeling of Intergranular Corrosion Damage,” *J Electrochem Soc,* vol. 165, no. 7, pp. C362-C374, 2018.

[27] G. F. Zhang, G. A. Gazonas, and F. Bobaru, “Supershear damage propagation and sub-Rayleigh crack growth from edge-on impact: A peridynamic analysis,” *Int J Impact Eng,* vol. 113, pp. 73-87, 2018.

[28] S. Jafarzadeh, Z. Chen, and F. Bobaru, “Peridynamic modeling of repassivation in pitting corrosion of stainless steel,” *Corros.,* vol. 74, no. 4, pp. 393-414, 2017.

[29] M. Behzadinasab, T. J. Vogler, A. M. Peterson, R. Rahman, and J. T. Foster, “Peridynamics Modeling of a Shock Wave Perturbation Decay Experiment in Granular Materials with Intra-granular Fracture,” *J Dyn Behav M.*, pp. 1-14, 2018.

[30] M. Radel, C. Willberg, and D. Krause, “Peridynamic analysis of fibre-matrix debond and matrix failure mechanisms in composites under transverse tensile load by an energy-based damage criterion,” *Composites Part B-Engineering,* vol. 158, pp. 18-27, 2019.

[31] F. Bobaru, J. Mehrmashadi, Z. Chen, and S. Niazi, “Intraply Fracture in Fiber-reinforced Composites: A Peridynamic Analysis,” in ASC 33rd Annual Technical Conference & 18th US-Japan Conference on Composite Materials, Seattle, 2018, pp. 9.

[32] Z. Chen, S. Niazi, G. Zhang, and F. Bobaru, "Peridynamic Functionally Graded and Porous Materials: Modeling Fracture and Damage,"in *Handbook of Nonlocal Continuum Mechanics for Materials and Structures*, G. Z. Voyiadjis, ed., pp. 1-35: Springer International Publishing, 2017. DOI: 10.1007/978-3-319-22977-5_36-1

[33] S. A. Silling, "Reformulation of elasticity theory for discontinuities and long-range forces," *J Mech Phys Solids,* vol. 48, no. 1, pp. 175-209, 2000.

[34] S. Jafarzadeh, Z. Chen, J. Zhao, and F. Bobaru, "Pitting, lacy covers, and pit merger in stainless steel: 3D peridynamic models," *Corrosion Science*, 2019.

[35] J. Zhao, Z. Chen, J. Mehrmashhadi, and F. Bobaru, "Construction of a peridynamic model for transient advection-diffusion problems," *Int J Heat Mass Transfer,,* vol. 126, pp. 1253-1266, 2018.

[36] S. A. Silling, and F. Bobaru, "Peridynamic modeling of membranes and fibers," *INT J NONLINEAR MECH.,* vol. 40, no. 2-3, pp. 395-409, 2005.

[37] S. A. Silling, and E. Askari, "A meshfree method based on the peridynamic model of solid mechanics," *Comput Struct.,* vol. 83, no. 17-18, pp. 1526-1535, 2005.

[38] Y. Ha, and F. Bobaru, "Studies of dynamic crack propagation and crack branching with peridynamics," *Int. J Fracture.,* vol. 162, no. 1-2, pp. 229-244, 2010.

[39] G. Zhang, and F. Bobaru, "Modeling the evolution of fatigue failure with peridynamics," *Rom J Tech Sci Appl Mech.,* vol. 66, pp. 20-39, 2016.

[40] D. J. Littlewood, *Roadmap for Peridynamic Software Implementation,* SANDIA REPORT SAND2015-9013, S. N. L. (SNL - NM), Albuquerque, NM, USA, 2015.

[41] Z. Xu, G. Zhang, Z. Chen, and F. Bobaru, "Elastic vortices and thermally-driven cracks in brittle materials with peridynamics," *Int. J Fracture.,* vol. 209, no. 1-2, pp. 203-222, 2017.

[42] J. R. Shewchuk, *An introduction to the conjugate gradient method without the agonizing pain,* Technical Report CMUCS-TR-94-125, Carnegie-Mellon University. Department of Computer Science, 1994.

[43] Y. H. Dai, and Y. Yuan, "An efficient hybrid conjugate gradient method for unconstrained optimization," *Ann Oper Res.,* vol. 103, no. 1-4, pp. 33-47, 2001.

[44] S. Li, Z. Chen, L. Tan, and F. Bobaru, "Corrosion-induced embrittlement in ZK60A Mg alloy," *Mater Sci Eng A,* vol. 713, pp. 7-17, 2018.

[45] Q. Le, and F. Bobaru, "Surface corrections for peridynamic models in elasticity and fracture," *Comput Mech,* vol. 61, no. 4, pp. 499-518, 2018.

[46] W. K. Hu, Y. D. Ha, and F. Bobaru, "Modeling Dynamic Fracture and Damage in a Fiber-Reinforced Composite Lamina with Peridynamics," *Int J Multiscale Comput Eng.,* vol. 9, no. 6, pp. 707-726, 2011.

[47] H. Ahmadian, B. Liang, and S. Soghrati, "An integrated computational framework for simulating the failure response of carbon fiber reinforced polymer composites," *Comput Mech,* vol. 60, no. 6, pp. 1033-1055, 2017.

[48] M. Duzzi, M. Zaccariotto, and U. Galvanetto, "Application of peridynamic theory to nanocomposite materials," *Adv Mat Research,* vol. 1016, pp. 44-48, 2014.

[49] D. Dipasquale, M. Zaccariotto, and U. Galvanetto, "Crack propagation with adaptive grid refinement in 2D peridynamics," *Int. J Fracture.,* vol. 190, no. 1, pp. 1-22, 2014.

[50] W. K. Hu, Y. D. Ha, and F. Bobaru, "Peridynamic model for dynamic fracture in unidirectional fiber-reinforced composites," *Comput Methods Appl Mech Eng,* vol. 217, pp. 247-261, 2012.

[51] C. Gonzalez, J. Llorca, and A. Weck, "Toughness of fiber-reinforced titanium as a function of temperature: experimental results and micromechanical modeling," *Acta Mater.,* vol. 52, no. 13, pp. 3929-3939, 2004.

[52] E. Totry, C. Gonzalez, J. LLorca, and J. M. Molina-Aldareguia, “Mechanisms of shear deformation in fiber-reinforced polymers: experiments and simulations,” *Int. J Fracture.,* vol. 158, no. 2, pp. 197-209, 2009.

[53] Z. Chen, S. Niazi, and F. Bobaru, “A peridynamic model for damage and fracture in porous materials,” *International Journal of Rock Mechanics and Mining Sciences*, 2019 (under Review).

[54] K. Makarian, and S. Santhanam, "Utility of 2D Finite Element Simulations for Predicting Effective Thermomechanical Properties of Particle-Reinforced Composites," Proceedings of the ASME 2018 International Mechanical Engineering Congress and Exposition, Pittsburgh, PA, USA, 2018.

[55] F. Bobaru, and W. K. Hu, “The Meaning, Selection, and Use of the Peridynamic Horizon and its Relation to Crack Branching in Brittle Materials,” *Int. J Fracture.,* vol. 176, no. 2, pp. 215-222, 2012.

[56] S. Silling, “Fragmentation modeling with EMU,” *Sandia National Laboratories, Albuquerque, NM, Technical report*, 2005.

[57] Y. D. Ha, and F. Bobaru, “Characteristics of dynamic brittle fracture captured with peridynamics,” *Eng Fract Mech,* vol. 78, no. 6, pp. 1156-1168, 2011.

[58] G. F. Zhang, Q. Le, A. Loghin, A. Subramaniyan, and F. Bobaru, “Validation of a peridynamic model for fatigue cracking,” *Eng Fract Mech,* vol. 162, pp. 76-94, 2016.

[59] "CUDA Zone," https://developer.nvidia.com/cuda-zone.

[60] G. Sarego, Q. V. Le, F. Bobaru, M. Zaccariotto, and U. Galvanetto, “Linearized state‐based peridynamics for 2‐D problems,” *International Journal for Numerical Methods in Engineering,* vol. 108, no. 10, pp. 1174-1197, 2016.